Geophysical Journal International

Geophys. J. Int. (2017) **211,** 512–527
Advance Access publication 2017 August 2
GJI Seismology

doi: 10.1093/gji/ggx318

Synthesis of a scalar wavelet intensity propagating through von Kármán-type random media: joint use of the radiative transfer equation with the Born approximation and the Markov approximation

Haruo Sato and Kentaro Emoto

Geophysics, Science, Tohoku University, Aoba-ku, Sendai-shi, Miyagi-ken 980-8578, *Japan. E-mail: satoharuo@m.tohoku.ac.jp*

Accepted 2017 July 28. Received 2017 July 22; in original form 2017 March 3

SUMMARY

In high-frequency seismograms of small earthquakes, we clearly see the excitation of long lasting coda waves and the envelope broadening of an *S*-wavelet with travel distance increasing. We can interpret those phenomena resulting from scattering by random inhomogeneities distributed in the earth medium. Those phenomena have been theoretically studied by stochastic methods, which deal with velocity inhomogeneities as random media. As a simple mathematical model, we study the propagation of a scalar wavelet for the spherical radiation from a point source in 3-D von Kármán-type random media, of which the power spectral density function (PSDF) decreases according to a power-law higher than the corner wavenumber. Our objective is to propose a method to synthesize the wavelet intensity time trace, the mean square amplitude trace, at a given travel distance by using statistical parameters characterizing the PSDF and the centre wavenumber of the wavelet. When the phase shift is small, we can use the Born approximation to calculate the non-isotropic scattering coefficient representing the scattering power per unit volume. Using the scattering coefficient in the radiative transfer equation (RTE), we are able to synthesize the wavelet intensity time trace. When the centre wavenumber increases in the power-law spectral range, however, we often face the situation of a large phase shift, where the Born approximation is inapplicable, but we are able to use the Markov approximation based on the parabolic approximation. It well explains the intensity time traces showing envelope broadening with peak delay due to multiple scattering around the forward direction and the wandering effect caused by travel time fluctuations; however, it fails to explain rich coda waves composed of scattered waves in wide angles. In such a case, here, we newly propose the spectrum division method as follows: at first, taking the centre wavenumber with a tuning parameter as a reference, we divide the random medium spectrum into the low- and high-wavenumber spectral (long- and short-scale) components. The second step is to synthesize the intensity time-trace by using the RTE with the Born scattering coefficient for the short-scale component. The third step is to calculate the envelope broadening and the wandering effects due to the long-scale component. As the fourth step, at each travel distance, we convolve the intensity time trace calculated by the RTE with the envelope broadening and wandering effects and the source function, which gives the intensity time trace reflecting the scattering contribution of all the spectral components. In parallel, realizing random media for given statistical parameters, we conduct finite difference (FD) simulations of waves through them for the spherical radiation of a Ricker wavelet from a point source. We confirm that synthesized intensity time traces well explain averaged FD simulation intensity traces from the onset through the peak to coda for a specific case. Those syntheses will be a theoretical basis for the study of random velocity inhomogeneities in the earth medium from the analysis of high-frequency seismic waves of small earthquakes.

Key words: Acoustic properties; Coda waves; Seismic attenuation; Theoretical seismology; Wave propagation; Wave scattering and diffraction.

1 INTRODUCTION

In high-frequency seismograms of small earthquakes, long lasting coda waves appear after the direct arrival and the *S*-wavelet shows peak delay from the onset and envelope broadening with travel distance increasing. Those phenomena have been investigated as results of scattering by random inhomogeneities distributed in the solid earth medium (e.g. Aki & Chouet 1975; Kopnichev 1975; Sato 1977; Rautian & Khalturin 1978; Sato 1984, 1989; Hoshiba *et al.* 1991; Zeng *et al.* 1991; Gusev & Abubakirov 1996). There have been many studies putting focus on the smooth variation of wave intensity, mean square (MS) envelope, disregarding their complex phase variation. Wave propagation through inhomogeneous media of small fractional velocity fluctuations has been theoretically studied by introducing an ensemble of random media (e.g. Chernov 1960; Rytov *et al.* 1989; Ishimaru 1997; Margerin 2005), where random media are statistically characterized by their power spectral density function (PSDF).

In most cases, the PSDF of random media is often supposed to be a Gaussian-type spectrum or a von Kármán-type spectrum having a power-law decay at large wavenumbers. The former is mathematically tractable, however, the latter is more suitable as a model representing the real earth medium. In the shallow crust, measurements of acoustic well-log data clearly reveal a power-law decay spectrum, where the exponent of the power-law decay varies depending on lithological condition and the power-law spectral range strongly depends on the sample length (e.g. Wu *et al.* 1994; Holliger 1996; Shiomi *et al.* 1997). Peak delay measurements of *S*-wave envelopes of regional earthquakes have revealed that the exponent of the power-law decay in the lithosphere, especially beneath active volcanoes, varies in relation with seismotectonic setting (e.g. Obara & Sato 1995; Gusev & Abubakirov 1999; Petukhin & Gusev 2003; Takahashi *et al.* 2007, 2009; Tripathi *et al.* 2010). The PSDF of random velocity inhomogeneity in the solid earth is different from the Kolmogorov spectrum of the refractive index fluctuation of the atmosphere that has a constant exponent $-11/3$ (e.g. Andrews & Phillips 2005). Estimated characteristic scales of randomness are less than 1 km in the crust (e.g. Yoshimoto *et al.* 1997; Sens-Schönfelder *et al.* 2009; Calvet & Margerin 2013); however, they are longer than 1 km or more in the lithosphere and the upper mantle (e.g. Shearer & Earle 2004; Saito *et al.* 2005; Mancinelli *et al.* 2016). Those observations suggest that it seems natural to use von Kármán-type random media as a plausible model of random velocity inhomogeneities in the solid earth.

As a simple mathematical model, we study the propagation of a scalar wavelet with a centre wavenumber k_c for the spherical radiation from a point source in 3-D von Kármán-type random media of order κ with the average velocity V_0. Their PSDF is characterized by a small MS fractional fluctuation $\varepsilon^2 \ll 1$ and a corner wavenumber at a^{-1}. The PSDF obeys a power-law $m^{-2\kappa-3}$ for wavenumber $m \gg a^{-1}$. Our objective is to propose a method to synthesize wavelet intensity time traces at a given travel distance by using statistical parameters ε^2, a, κ, V_0 and k_c.

We often use the Born approximation to calculate the scattering coefficient representing the scattering power per unit volume. Using the scattering coefficient in the radiative transfer equation (RTE), we are able to calculate the intensity time traces that reflect multiple non-isotropic scattering effect (e.g. Hoshiba 1995; Gusev & Abubakirov 1996; Haney *et al.* 2005; Margerin 2005; Wegler *et al.* 2006; Przybilla & Korn 2008; Sens-Schönfelder *et al.* 2009; Calvet & Margerin 2013). Practical calculation is done by using the Monte Carlo simulation method. Good coincidence between synthesized intensity traces with those calculated from FD simulations is reported (e.g. Wegler *et al.* 2006; Przybilla & Korn 2008).

Taking the scattering of a plane wave with wavenumber k_c by a single high-velocity sphere with radius a and velocity $V_0(1+\varepsilon)$ in a homogenous medium with velocity V_0, where $\varepsilon \ll 1$, we recall the applicable condition of the Born approximation. The basic assumption is a smallness of the phase shift in the scattering obstacle, which is always valid when $ak_c \ll 1$; however, we have to seriously consider the phase shift in the obstacle as ak_c increases. According to the distorted Born approximation based on the parabolic approximation, the phase shift at the centre of the obstacle is εak_c (e.g. Landau & Lifshitz 2003, p. 543). It means that the Born approximation is applicable if $\varepsilon^2 a^2 k_c^2 \ll 1$. Speculating from the above study, even for scattering through random media, we may say that the Born approximation is applicable in the RTE only when $\varepsilon^2 a^2 k_c^2 \ll 1$. The same condition is necessary for the derivation of the RTE from the Bethe–Salpeter equation for random media by using the Bourret approximation for the ladder approximation (e.g. Rytov *et al.* 1989, p. 151)

When the centre wavenumber is in the power-law spectral range, $ak_c > 1$, we often face the situation where $\varepsilon^2 a^2 k_c^2$ becomes the order of 1 or larger, which is abbreviated as $\varepsilon^2 a^2 k_c^2 \gtrsim O(1)$. In such a case, we can calculate the wave intensity trace using the Markov approximation, which is a stochastic extension of the phase screen method on the basis of the parabolic approximation (e.g. Williamson 1972; Shishov 1974; Lee & Jokipii 1975a,b; Sreenivasiah *et al.* 1976; Sato 1989, 2008; Fehler *et al.* 2000; Saito *et al.* 2002; Korn & Sato 2005; Emoto *et al.* 2010; Sawazaki *et al.* 2011; Emoto *et al.* 2012). This method well explains the peak delay from the onset and the envelope broadening of the wavelet produced by successive multiple scattering in a narrow angle around the forward direction; however, this method has difficulty in explaining rich coda waves composed of scattered waves into wide angles.

Here, we propose a new method, which will be referred to the spectrum division method, to synthesize intensity time traces especially for the case of $ak_c > 1$ and $\varepsilon^2 a^2 k_c^2 \gtrsim O(1)$ as follows: The first step is to divide the random medium spectrum into the low- and high-wavenumber spectral (long- and short-scale) components by taking ζk_c as a reference, where ζ is a tuning parameter (Sato 2016, refer to Paper I in the following). The second step is to synthesize the intensity time-trace by using the RTE with the Born scattering coefficient for the short-scale component. The third step is to calculate the envelope broadening effect and wandering effect due to the long-scale component by using the Markov approximation. The fourth step is to convolve the envelope broadening and wandering effects with the intensity trace calculated by the RTE in the previous step and the source function in the time domain. The obtained intensity traces reflect all the scattering contribution of

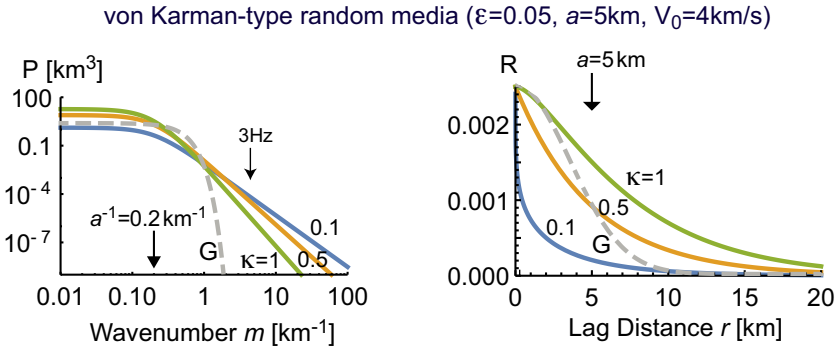

Figure 1. Log–log plot of PSDF versus wavenumber (left), and linear plot of ACF versus lag distance (right) for von Kármán-type random media. Grey broken lines are Gaussian-type for a comparison.

the whole spectrum of random media. Then, we compare synthesized intensity time traces for a Ricker wavelet source with those calculated by using FD simulations. At the end, we discuss unsolved problems and possible developments.

2 SCALAR WAVES IN VON KÁRMÁN-TYPE RANDOM MEDIA

2.1 Scalar wave equation

Scalar wave $u(\boldsymbol{x}, t)$ is governed by the wave equation for a medium characterized by wave velocity $V(\boldsymbol{x}) = V_0(1 + \xi(\boldsymbol{x}))$:

$$\Delta u - \frac{1}{V_0^2}\partial_t^2 u + \frac{2}{V_0^2}\xi\partial_t^2 u = 0, \tag{1}$$

where V_0 is the average velocity and ξ is a random fractional fluctuation. If there is a source radiation, we put the source term on the right-hand side. We imagine an ensemble of random media $\{\xi\}$, where $\langle\xi\rangle = 0$. Angular brackets $\langle ...\rangle$ mean an ensemble average. Randomness is supposed to be statistically homogeneous, isotropic and small, $\varepsilon^2 \equiv \langle\xi^2\rangle \ll 1$. We statistically study the propagation of the intensity $\langle u^2\rangle$ of a wavelet with the centre wavenumber $k_c = \omega_c/V_0$ through random media. Paper I studied the energy density $\langle\dot{u}^2\rangle$, which is equal to $\omega_c^2\langle u^2\rangle$ for monochromatic waves.

2.2 von Kármán-type random media

The PSDF of von Kármán-type random media of order κ is given by

$$P(\kappa, \boldsymbol{m}) = P(\kappa, m) = \frac{8\pi^{\frac{3}{2}}\Gamma\left(\kappa+\frac{3}{2}\right)\varepsilon^2 a^3}{\Gamma(\kappa)(1+a^2m^2)^{\kappa+\frac{3}{2}}} \quad \text{for} \quad \kappa > 0, \tag{2a}$$

which shows a power-law decay at wavenumbers higher than the corner at a^{-1}. Its Fourier transform, the autocorrelation function (ACF) is

$$R(\kappa, \boldsymbol{x}) = R(\kappa, r) = \frac{2^{1-\kappa}}{\Gamma(\kappa)}\varepsilon^2\left(\frac{r}{a}\right)^{\kappa} K_{\kappa}\left(\frac{r}{a}\right) \quad \text{for} \quad \kappa > 0, \tag{2b}$$

where K_{κ} denotes a Bessel function of the second kind, and $\varepsilon^2 = R(\kappa, 0)$.

Fig. 1 shows PSDF's and ACF's for different κ values, where an arrow indicates the wavenumber k_c for the frequency $f_c = 3$ Hz as an example. We will use $\varepsilon = 0.05$, $a = 5$ km and $V_0 = 4$ km s^{-1} in the following simulations. At large wavenumbers, the PSDF for $\kappa = 1$ is smaller than that for $\kappa = 0.1$; however, it is still larger than the Gaussian PSDF (grey broken line). The ACF for $\kappa = 1$ shows a smooth variation near the zero lag-distance; however, the ACF for $\kappa = 0.1$ has a sharp peak at zero lag-distance.

3 STOCHASTIC SYNTHESIS OF INTENSITY TIME TRACE

3.1 Radiative transfer equation using the Born scattering coefficient

3.1.1 Radiative transfer equation

For spherical (isotropic) and impulsive radiation from a point source at the origin in a 3-D scattering medium, the directional distribution of intensity f of centre wavenumber k_c to direction $\boldsymbol{q}$ at $(\boldsymbol{x}, t)$, where $|\boldsymbol{q}| = 1$, is governed by the following differential and integral RTE

(e.g. Ishimaru 1997, eq. 7.30) :

$$\partial_t f(k_c, \boldsymbol{x}, t, \boldsymbol{q}) + V_0 \boldsymbol{q} \nabla f(k_c, \boldsymbol{x}, t, \boldsymbol{q}) = -g_0(k_c) V_0 f(k_c, \boldsymbol{x}, t, \boldsymbol{q}) + \frac{V_0}{4\pi} \oint g\left(k_c, \psi(\boldsymbol{q}, \boldsymbol{q}')\right) f\left(k_c, \boldsymbol{x}, t; \boldsymbol{q}'\right) \mathrm{d}\Omega_{q'} + \frac{1}{4\pi} \delta(\boldsymbol{x}) \delta(t), \tag{3}$$

where $g(k_c, \psi(\boldsymbol{q}, \boldsymbol{q}'))$ is a scattering coefficient as a function of scattering angle ψ between $\boldsymbol{q}$ and $\boldsymbol{q}'$. Symbol $\mathrm{d}\Omega_{q'}$ is a solid angle element to direction $\mathbf{q}'$, and $g_0(k_c) \equiv \frac{1}{4\pi} \oint g(k_c, \psi(\boldsymbol{q}, \boldsymbol{q}'))\mathrm{d}\Omega_{q'}$ is the total scattering coefficient. The left-hand side shows an advection equation, and three terms in the right-hand side represent the scattering loss, sum of scattering contributions from different directions, and the isotropic unit source radiation. The integral of f over solid angle gives the intensity propagator of the scattering medium:

$$G_R(k_c, \boldsymbol{x}, t) \equiv \oint f(k_c, \boldsymbol{x}, t; \mathbf{q}) \, \mathrm{d}\Omega_q. \tag{4}$$

The space integral is always conserved, $\iiint_{-\infty}^{\infty} \mathrm{d}\boldsymbol{x} G_R(\kappa, k_c, \boldsymbol{x}, t) = 1$. The resultant G_R contains both coherent wavelet (direct wavelet) intensity and scattered wave intensity.

RTE (3) can be written as an integral equation (Sato 1995; Sato *et al.* 2012, eqs 790, 7.91):

$$f(k_c, \boldsymbol{x}, t, \boldsymbol{q}) = G(k_c, \boldsymbol{x}, t, \boldsymbol{q}) + V_0 \int_{-\infty}^{\infty} \mathrm{d}t' \iiint_{-\infty}^{\infty} \mathrm{d}\boldsymbol{x}' \oint \mathrm{d}\Omega_{q'} G(k_c, \boldsymbol{x} - \boldsymbol{x}', t - t', \boldsymbol{q}) g(k_c, \psi(\boldsymbol{q}, \boldsymbol{q}')) f(k_c, \boldsymbol{x}', t', \boldsymbol{q}'), \tag{5}$$

where the propagator

$$G(k_c, \boldsymbol{x}, t; \boldsymbol{q}) = \delta_\Omega(\boldsymbol{q}, \boldsymbol{x}) e^{-g_0(k_c) V_0 t} G_0(\boldsymbol{x}, t) \tag{6}$$

is composed of a delta function for solid-angle δ_Ω, an exponential scattering loss term, and a causal propagator of a ballistic wave intensity with a constant velocity V_0,

$$G_0(\boldsymbol{x}, t) = \frac{1}{4\pi r^2 V_0} \delta\left(t - \frac{r}{V_0}\right) H(t). \tag{7}$$

3.1.2 Link between random media and a scattering medium

There is a mathematical link between the RTE for a scattering medium and the wave equation for random media. The RTE can be derived from the Bethe–Salpeter equation based on the Bourret approximation for the ladder approximation (e.g. Rytov *et al.* 1989; Margerin 2005), or from the smoothing approximation with multiscale analysis (e.g. Howe 1973, 1974; Sato *et al.* 2012). The key parameter of the RTE (3) is the scattering coefficient g as a function of scattering angle ψ and wavenumber k_c. When $ak_c < 1$, we can use the Born approximation to derive the scattering coefficient g from the PSDF of random media (Chernov 1960; Aki & Chouet 1975; Sato *et al.* 2012). Even when $ak_c > 1$, the Born approximation is still applicable if the phase shift across the inhomogeneity is small:

$$\varepsilon^2 a^2 k_c^2 \ll 1. \tag{8}$$

The scattering coefficient is given by

$$g(\kappa, k_c, \psi) = \frac{k_c^4}{\pi} P\left(\kappa, 2k_c \sin\frac{\psi}{2}\right) = \frac{8\pi^{1/2}\Gamma(\kappa + 3/2)\varepsilon^2 \, a^3 k_c^4}{\Gamma(\kappa)\left(1 + 4a^2 k_c^2 \sin^2\frac{\psi}{2}\right)^{\kappa+3/2}} \approx \frac{8\pi^{1/2}\Gamma(\kappa + 3/2)\varepsilon^2 \, a^3 k_c^4}{\Gamma(\kappa)\left(1 + a^2 k_c^2 \psi^2\right)^{\kappa+3/2}} \quad \text{for} \quad \psi \ll 1. \tag{9}$$

It takes the maximum value into the forward direction $\psi = 0$, and rapidly decreases as ψ increases beyond the corner at $(ak_c)^{-1}$. The forward scattering $g(\kappa, k_c, \psi = 0)$ increases as ak_c increases. The total scattering coefficient is the average of g over solid angle:

$$g_0(\kappa, k_c) = \frac{1}{4\pi} \int_0^{2\pi} d\varphi \int_0^{\pi} \sin\psi \mathrm{d}\psi \; g(\kappa, k_c, \psi) = \frac{k_c^2}{2\pi} \int_0^{2k_c} P(\kappa, m) m \mathrm{d}m = \frac{4\pi^{1/2}\Gamma(\kappa + 3/2)\varepsilon^2 \, a k_c^2}{\Gamma(\kappa) 2(\kappa + 1/2)} \left[1 - \frac{1}{(1 + 4a^2 k_c^2)^{\kappa+1/2}}\right], \tag{10}$$

which increases with k_c increasing. Inserting (9) and (10) into the RTE (3), we calculate $f(\kappa, k_c, \boldsymbol{x}, t, \boldsymbol{q})$ and then $G_R(\kappa, k_c, \boldsymbol{x}, t)$, where argument κ is added. Those are functions of $r \equiv |\boldsymbol{x}|$ since the source radiation is isotropic.

We note that the RTE describes ray bending processes only; however, the RTE does not consider the wandering effect caused by travel time fluctuations, which is naturally derived along with the Markov approximation (Sato *et al.* 2012, eq. 9.75). The characteristic time width of the wandering effect at distance r is

$$t_W(\kappa, k_c, r) = \frac{\sqrt{2A(\kappa, 0) r}}{V_0}, \tag{11}$$

where A is the longitudinal integral of ACF as a function of transverse distance $r_\perp \equiv |\boldsymbol{x}_\perp|$:

$$A(\kappa, r_\perp) \equiv \int_{-\infty}^{\infty} R(\kappa, \boldsymbol{x}_\perp, z) \mathrm{d}z = \frac{2^{-\kappa+3/2}\sqrt{\pi}\varepsilon^2 a}{\Gamma(\kappa)} \left(\frac{r_\perp}{a}\right)^{\kappa+1/2} K_{\kappa+1/2}\left(\frac{r_\perp}{a}\right),$$

$$A(\kappa, r_\perp = 0) = \frac{2\pi^{1/2}\Gamma(\kappa + 1/2)}{\Gamma(\kappa)} \varepsilon^2 a. \tag{12}$$

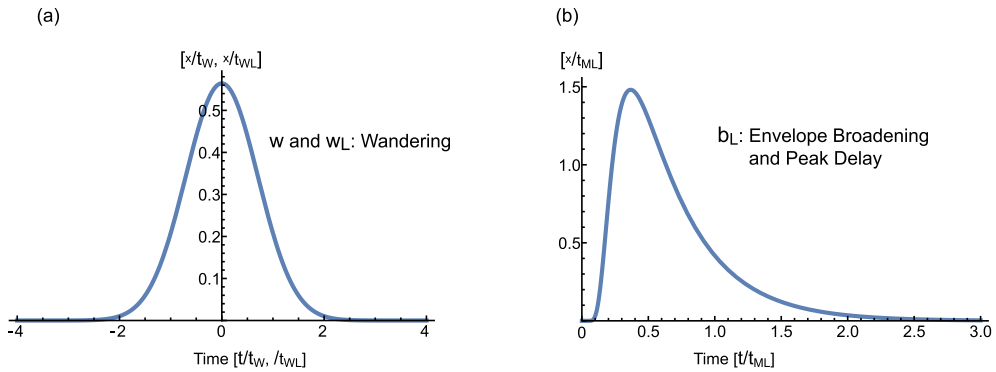

Figure 2. (a) Plot of the wandering term w versus time scaled by t_W, and w_L versus time scaled by t_{WL}, respectively. (b) Plot of the envelope broadening term with peak delay b_L versus time scaled by t_{ML}.

It leads to $t_W \propto \varepsilon(ar)^{1/2}/V_0$. The wandering effect is a Gaussian form in time,

$$w(\kappa, k_c, r, t) = \frac{1}{\sqrt{\pi}\ t_W(\kappa, k_c, r)} e^{-\frac{t^2}{t_W(\kappa,k_c,r)^2}}. \tag{13}$$

We note $\int_{-\infty}^{\infty} w(t)\mathrm{d}t = 1$. Fig. 2(a) shows a plot of w versus time scaled by t_W.

The objective propagator is given by the convolution of the propagator G_R with the wandering effect w in the time domain:

$$G_{w,R}(\kappa, k_c, r, t) = w(\kappa, r, t) \otimes G_R(\kappa, k_c, r, t). \tag{14}$$

By using the convolution of $G_{w,R}$ and the source function $s(k_c, t)$, we have the intensity time trace,

$$I_{w,R}(\kappa, k_c, \zeta, r, t) = G_{w,R}(\kappa, k_c, r, t) \otimes s(k_c, t). \tag{15}$$

The wandering term is a pure statistical effect which is necessary for the interpretation of the ensemble averaged intensity. Przybilla & Korn (2008) precisely studied the necessity of the above convolution.

3.2 Spectrum division method: joint use of the RTE with the Born approximation and the Markov approximation

When $ak_c \gg 1$, we often face the situation where $\varepsilon^2 a^2 k_c^2 \gtrsim O(1)$. In that case, the Born approximation is inapplicable. Here, we newly propose the spectrum division method as follows.

3.2.1 Decomposition of the random medium spectrum: the first step

According to Paper I, taking wavenumber ζk_c as a reference, where ζ is a tuning parameter, we decompose the random medium spectrum into low- and high-wavenumber spectral (long- and short-scale) components: $P(\boldsymbol{m}) = P_L(\boldsymbol{m}) + P_S(\boldsymbol{m})$ (see Paper I, eqs 5a–6b). We first define the short-scale component $P_S(\boldsymbol{m})$ as von Kármán-type with the same κ as

$$P_S(\kappa, k_c, \zeta, m) \equiv \frac{8\pi^{3/2}\Gamma(\kappa+3/2)\varepsilon_S^2\, a_S{}^3}{\Gamma(\kappa)\,(1+a_S{}^2m^2)^{\kappa+3/2}} = \frac{8\pi^{3/2}\Gamma(\kappa+3/2)\varepsilon^2\, a^3}{\Gamma(\kappa)\,((\zeta ak_c)^2+a^2m^2)^{\kappa+3/2}}. \tag{16a}$$

Its RMS fractional fluctuation and corner are

$$\varepsilon_S(\varepsilon, a, \kappa, \zeta, k_c) = \frac{\varepsilon}{(\zeta ak_c)^\kappa} \quad \text{and} \quad a_S(\zeta, k_c) = \frac{1}{\zeta k_c}, \tag{16b}$$

where $(ak_c)^{-1} < \zeta \le 1$. P_S increases and approaches P as ζ decreases. The corresponding ACF is

$$R_S(\kappa, k_c, \zeta, r) \equiv \frac{\varepsilon_S^2\, 2^{1-\kappa}}{\Gamma(\kappa)} \left(\frac{r}{a_S}\right)^\kappa K_\kappa\left(\frac{r}{a_S}\right) = \frac{\varepsilon^2\, 2^{1-\kappa}}{\Gamma(\kappa)(\zeta ak_c)^{2\kappa}} (\zeta k_c r)^\kappa\, K_\kappa(\zeta k_c r). \tag{16c}$$

Then, we calculate the PSDF and ACF of the long-scale component using $P_L = P - P_S$ and $R_L = R - R_S$, which are not von Kármán-type. We note that P_L has little high-wavenumber spectra, but P_S still has spectra at low wavenumbers.

3.2.2 Born approximation for the short-scale component: the second step

We can use the Born approximation for the short-scale component P_S if ζ is chosen to satisfy the condition of the small phase shift:

$$\varepsilon_S^2 a_S^2 k_c^2 \equiv \frac{\varepsilon^2}{\zeta^2(\zeta ak_c)^{2\kappa}} \ll 1. \tag{17}$$

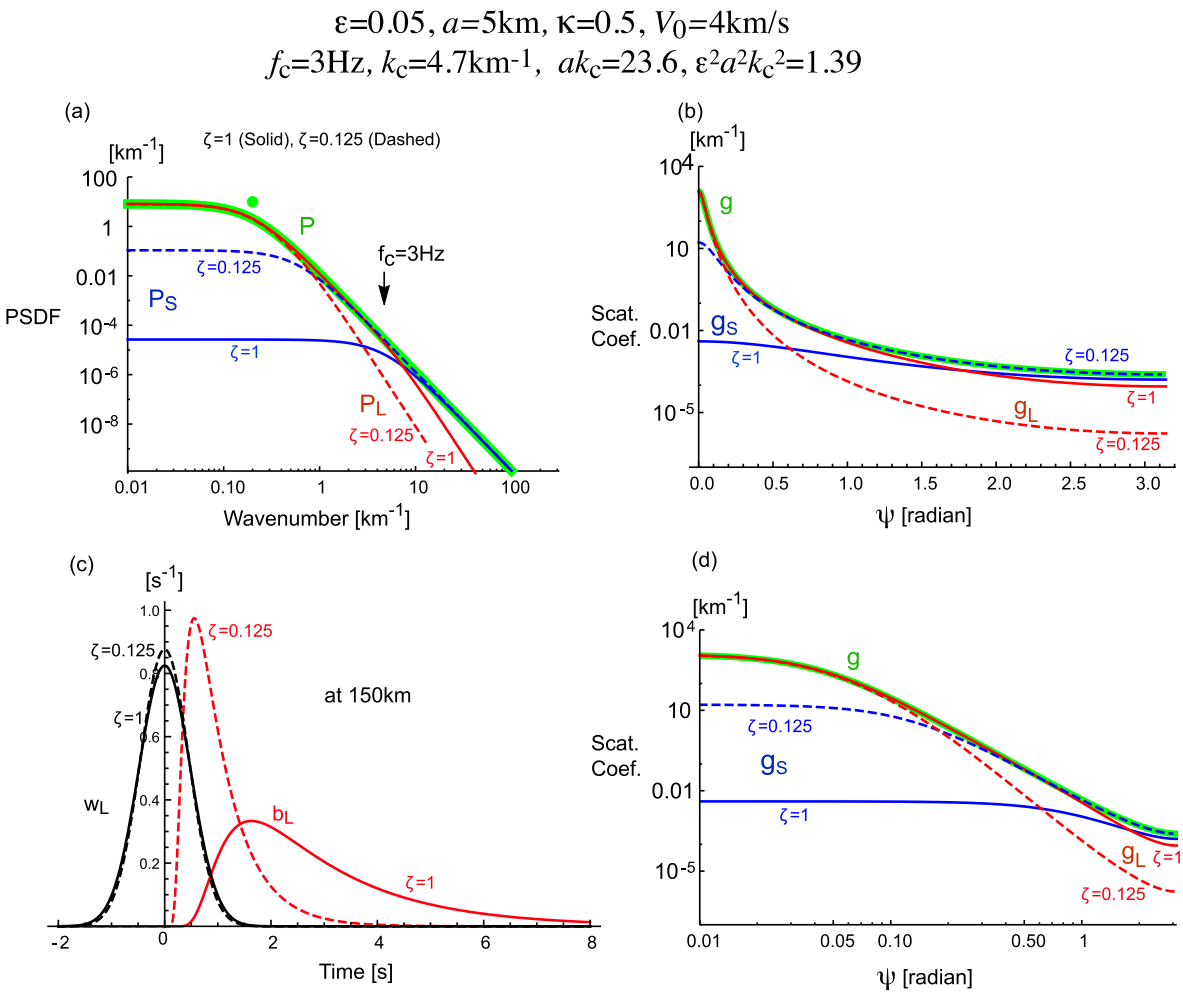

Figure 3. (a) Decomposition of P (green) into P_S (blue) and P_L (red) for $f_c = 3$ Hz. Semi-log plot (b) and log–log plot (d) of scattering coefficient versus scattering angle ψ: g (green) and g_S (blue) and g_L (red). (c) Broadening factor b_L (red) and wandering factor w_L (black) at 150 km. Solid and dashed lines are for $\zeta = 1.0$ and $\zeta = 0.125$, respectively.

For the von Kármán-type random media of ($\varepsilon = 0.05$, $\kappa = 0.5$, $a = 5$ km), at $f_c = 3$ Hz, $k_c = 4.71\,\text{km}^{-1}$ (arrow) is in the power-law range of P (green) as shown in Fig. 3(a) since $ak_c = 23.6 \gg 1$. The direct use of the Born approximation is inapplicable since $\varepsilon^2 a^2 k_c^2 = 1.39$. As examples, we show two cases of the spectrum decomposition: $\varepsilon_S^2 a_S^2 k_c^2 = 0.00011$ for $\zeta = 1.0$ and $\varepsilon_S^2 a_S^2 k_c^2 = 0.054$ for $\zeta = 0.125$. Both satisfy condition (17). Blue and red curves show P_S and P_L, respectively. Solid and dashed curves are for ζ=1.0 and 0.125, respectively. $P_S(m) \approx P(m)$ and $P_L(m) \ll P(m)$ in the power-law range; however, $P_S(m) \ll P(m)$ at low wavenumbers.

Applying the Born approximation to P_S, we calculate the scattering coefficient of the short-scale component in the same manner as (9):

$$g_S(\kappa, k_c, \zeta, \psi) = \frac{k_c^4}{\pi} P_S\left(\kappa, k_c, \zeta, 2k_c \sin\frac{\psi}{2}\right)$$
$$= \frac{8\pi^{1/2}\Gamma(\kappa+3/2)\varepsilon^2\, a^3 k_c^4}{\Gamma(\kappa)\left((\zeta a k_c)^2 + 4a^2 k_c^2 \sin^2\frac{\psi}{2}\right)^{\kappa+3/2}} \approx \frac{8\pi^{1/2}\Gamma(\kappa+3/2)\varepsilon^2\, a^3 k_c^4}{\Gamma(\kappa)\left((\zeta a k_c)^2 + a^2 k_c^2 \psi^2\right)^{\kappa+3/2}} \quad \text{for} \quad \psi \ll 1. \tag{18a}$$

We define the scattering coefficient of the long-scale component as

$$g_L(\kappa, k_c, \zeta, \psi) = g(\kappa, k_c, \psi) - g_S(\kappa, k_c, \zeta, \psi). \tag{18b}$$

In Figs 3(b) and (d), we show semi-log and log-log plots of g (green), g_S (blue) and g_L (red) versus scattering angle ψ. We note that $g(\psi = 0)$ is extremely large. Fig. 3(d) shows that g (green) has a corner at $\psi = (ak_c)^{-1} \sim 0.042$; however, g_S (blue) has a corner at $\psi = \zeta$. We note $g_L \approx g$ and $g_S \ll g$ for small angles, but $g_S \approx g$ at large ψ. In the forward direction g_S for $\zeta = 0.125$ (blue-dashed) is larger than g_S for $\zeta = 1.0$ (blue-solid), however, both take nearly the same value at a large ψ. We have shown g and g_L only for comparison, and we do not use them in the following synthesis.

The total scattering coefficient of the short-scale component is

$$g_{S0}(\kappa, k_c, \zeta) = \frac{1}{4\pi}\int_0^{2\pi} d\varphi \int_0^{\pi} \sin\psi\, d\psi\, g_S(\kappa, k_c, \zeta, \psi) = \frac{\varepsilon^2}{a}\frac{2\pi^{1/2}\Gamma(\kappa+1/2)}{\Gamma(\kappa)}\left[1 - \frac{1}{(1+4\zeta^{-2})^{\kappa+1/2}}\right]\frac{(\zeta a k_c)^{1-2\kappa}}{\zeta^2}, \tag{18c}$$

(see Paper I, eq. 39). By substituting g_S for g and g_{S0} for g_0 in (3), the RTE for the directional distribution of intensity f_S for the short-scale component is given by

$$\partial_t f_S(\kappa, k_c, \zeta, \boldsymbol{x}, t, \boldsymbol{q}) + V_0 \boldsymbol{q} \nabla f_S(\kappa, k_c, \zeta, \boldsymbol{x}, t, \boldsymbol{q})$$
$$= -g_{S0}(\kappa, k_c, \zeta) V_0 f_S(\kappa, k_c, \zeta, \boldsymbol{x}, t, \boldsymbol{q}) + \frac{V_0}{4\pi} \oint g_S\left(\kappa, k_c, \zeta, \psi(\boldsymbol{q}, \boldsymbol{q}')\right) f_S\left(\kappa, k_c, \zeta, \boldsymbol{x}, t, \boldsymbol{q}'\right) \mathrm{d}\Omega_{q'} + \frac{1}{4\pi} \delta(\boldsymbol{x}) \delta(t). \tag{19}$$

The intensity propagator is given by

$$G_{R,S}(\kappa, k_c, \zeta, \boldsymbol{x}, t) \equiv \oint f_S(\kappa, k_c, \zeta, \boldsymbol{x}, t; \mathbf{q}) \mathrm{d}\Omega_q, \tag{20}$$

where $\iiint_{-\infty}^{\infty} \mathrm{d}\boldsymbol{x} G_{R,S}(\kappa, k_c, \zeta, \boldsymbol{x}, t) = 1$.

3.2.3 Markov approximation for the long-scale component: the third step

When $ak_c > 1$, we may use the parabolic/paraaxial approximation. If $\zeta < 1$, P_L is smaller than P at k_c (see Fig. 3(a)), which is more suitable for the parabolic approximation. We may approximate the longitudinal integral of R_L for a small $r_\perp$ as

$$A_L(\kappa, k_c, \zeta, r_\perp) \equiv \int_{-\infty}^{\infty} R_L(\kappa, k_c, \zeta, \boldsymbol{x}_\perp, z) \mathrm{d}z$$
$$\approx \begin{cases} \frac{\varepsilon^2 a\, 2\pi^{1/2}\Gamma\left(\kappa+\frac{1}{2}\right)}{\Gamma(\kappa)} \left[\left(1 - \frac{1}{(\zeta a k_c)^{2\kappa+1}}\right) - \left(1 - \frac{1}{(\zeta a k_c)^{2\kappa-1}}\right) \frac{1}{2(2\kappa-1)} \left(\frac{r_\perp}{a}\right)^2\right] & \text{for } \kappa \neq 1/2, \\ 2\varepsilon^2 a \left(1 - \frac{1}{(\zeta a k_c)^2}\right) - \left(\varepsilon^2 a \ln(\zeta a k_c)\right) \left(\frac{r_\perp}{a}\right)^2 & \text{for } \kappa = 1/2, \end{cases} \tag{21}$$

where $\zeta > (ak_c)^{-1}$ (see Paper I, eqs 22c, 23c). Using the Markov approximation for a quasi-monochromatic wavelet with the centre wavenumber k_c through the long-scale component, we derive the intensity time trace for the spherical radiation from a point source (see Paper I, section 3.2). The propagator for the long-scale component of random media is written as a convolution of the wandering term w_L caused by travel time fluctuations, the broadening term b_L caused by ray bending processes due to multiple scattering around the forward direction, and the causal propagator G_0 with a geometrical spreading factor and a constant velocity V_0 in the time domain (see Paper I, eqs 16, 33):

$$G_L(\kappa, k_c, \zeta, r, t) = w_L(\kappa, k_c, \zeta, r, t) \otimes b_L(\kappa, k_c, \zeta, r, t) \otimes G_0(r, t). \tag{22}$$

The envelope broadening term is given by

$$b_L(\kappa, k_c, \zeta, r, t) = \frac{\pi^2}{16\, t_{ML}(\kappa, k_c, \zeta, r)} \vartheta_4''\left(0, e^{-\frac{\pi^2}{4} \frac{t}{t_{ML}(\kappa, k_c, \zeta, r)}}\right) H(t), \tag{23}$$

where symbol $\vartheta_4''(v, q) \equiv \partial_v{}^2 \vartheta_4(v, q)$ means the second derivative of the elliptic theta function of the fourth kind with respect to the first argument v, and t_{ML} is the characteristic time of broadening. The time trace of b_L shows a curve having a delayed peak and a smoothly decaying tail. Fig. 2(b) shows a plot of b_L (red) versus time scaled by t_{ML}. The peak delay measured from the onset is about $0.37 t_{ML}$, and the maximum peak value is about $1.48/t_{ML}$. We note that $\int_0^\infty b_L(\kappa, \zeta, k_c, r, t) \mathrm{d}t = 1$. The characteristic time is derived from A_L at a small transverse distance $r_\perp$ (see Paper I, eqs 26, 30b):

$$t_{ML}(\kappa, k_c, \zeta, r) = \frac{r}{2V_0} \frac{1}{(a_{L\perp} k_c)^2} = \frac{\varepsilon^2}{2V_0 a} r^2 \times \begin{cases} \frac{\pi^{1/2}\Gamma\left(\kappa+\frac{1}{2}\right)}{(2\kappa-1)\Gamma(\kappa)} \left(1 - (\zeta a k_c)^{1-2\kappa}\right) & \text{for } \kappa \neq \frac{1}{2}, \\ \ln \zeta a k_c & \text{for } \kappa = \frac{1}{2}. \end{cases} \tag{24}$$

Peak delay and broadening given by b_L depend on f_c through t_{ML}, which shows what is called the stochastic dispersion (e.g. McLaughlin & Anderson 1987).

The Markov approximation for the intensity is valid when $a_{L\perp} k_c \gg 1$, where the coherence radius $a_{L\perp}$ at distance r is defined by $k_c^2 r(A_L(\kappa, k_c, \zeta, 0) - A_L(\kappa, k_c, \zeta, a_{L\perp})) = 1$ (Rytov *et al.* 1989, p. 110, eq. 3.114, Paper I, eqs 28, 37). It is equivalent to

$$t_{ML}(\kappa, k_c, \zeta, r) \ll \frac{r}{2V_0}. \tag{25}$$

This condition works as a constraint for the applicable travel distance range since $\frac{t_{ML}}{r/V_0} \propto \varepsilon^2 \frac{r}{a}$. Emoto *et al.* (2010) numerically examined this condition for the case of a Gaussian ACF.

The wandering term is directly calculated from $A_L(\kappa, k_c, \zeta, r_\perp = 0)$ as the same as (13):

$$w_L(\kappa, k_c, \zeta, r, t) = \frac{1}{\sqrt{\pi}\, t_{WL}(\kappa, k_c, \zeta, r)} e^{-\frac{t^2}{t_{WL}(\kappa, k_c, \zeta, r)^2}}, \tag{26}$$

where $\int_{-\infty}^{\infty} w_L(t) \mathrm{d}t = 1$. The characteristic time is

$$t_{WL}(\kappa, k_c, \zeta, r) = \frac{\sqrt{2A_L(\kappa, k_c, \zeta, 0) r}}{V_0} = \frac{2}{V_0} \sqrt{\varepsilon^2 a \frac{\pi^{1/2}\Gamma\left(\kappa+\frac{1}{2}\right)}{\Gamma(\kappa)} \left(1 - (\zeta a k_c)^{-2\kappa-1}\right)} \sqrt{r} \tag{27}$$

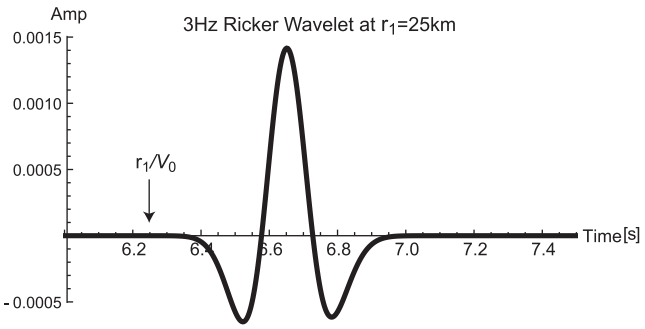

Figure 4. Waveform at a distance of 25 km for a Ricker wavelet source of $f_c = 3$ Hz in a homogeneous medium with $V_0 = 4\,\mathrm{km\ s^{-1}}$.

(Paper I, eqs 16, 24). Fig. 2(a) shows a plot of w_L versus time scaled by t_{WL}.

We show plots of b_L (red) versus time and w_L (black) versus time at a 150 km distance in Fig. 3(c). Difference between w_L for $\zeta = 0.125$ and that for $\zeta = 1.0$ is small; however, b_L for $\zeta = 1.0$ is more broadened than that for $\zeta = 0.125$. Figs 3(b) and (c) show how parameter ζ controls the relative contribution of the long and short scale components. When $\zeta = 0.125$, g_S is non-isotropic and b_L is narrow; however, when $\zeta = 1.0$, g_S is nearly isotropic and b_L is broadened.

We confirm $G_L \to G_0$ as $r \to 0$ since b_L and w_L approach a delta function as $r \to 0$. The time integral is independent of radius r, $\int_0^\infty 4\pi r^2 V_0\, G_L dt = 1$; however, we note $\int_0^\infty 4\pi r^2 G_L dr \neq 1$, which slightly destroys the energy conservation.

Convolution (22) means a redistribution of the propagation velocity, more correctly, as a redistribution of the slowness along the ballistic ray. Function w_L works as a symmetric smoothing filter and b_L works as an lag filter in the time domain.

3.2.4 Convolution of the RTE intensity and the wandering and broadening effects: the fourth step

We remember that $G_{R,S}$ represents the coherent (direct) wavelet intensity and the scattering contribution of P_S, however, the used propagator (7) has a constant velocity V_0. Since most of seismic rays of $G_{R,S}$ just after the onset propagate in a narrow angle around the forward direction, as an approximation, we propose to replace G_0 with $G_{R,S}$ in (22) at a given travel distance in order to define the propagator reflecting both scattering contribution of P_S and P_L :

$$G_{L,S}(\kappa, k_c, \zeta, r, t) = w_L(\kappa, k_c, \zeta, r, t) \otimes b_L(\kappa, k_c, \zeta, r, t) \otimes G_{R,S}(\kappa, \zeta, k_c, r, t)\,. \tag{28}$$

We expect this is a good approximation at least if characteristic times of the broadening term is very small compared with the travel time.

Convolution with the source function $s(k_c, t)$, we have the intensity time traces as

$$I_{L,S}(\kappa, k_c, \zeta, r, t) = G_{L,S}(\kappa, k_c, \zeta, r, t) \otimes s(k_c, t) = w_L(\kappa, k_c, \zeta, r, t) \otimes b_L(\kappa, k_c, \zeta, r, t) \otimes I_{R,S}(\kappa, k_c, \zeta, r, t), \tag{29a}$$

where

$$I_{R,S}(\kappa, k_c, \zeta, r, t) = G_{R,S}(\kappa, k_c, \zeta, r, t) \otimes s(k_c, t). \tag{29b}$$

Convolution with the wandering effect is always necessary when the synthesized intensity trace is compared with the ensemble averaged intensity, however, it is not necessary when synthesized intensity traces are compared with individual traces in one realization.

4 COMPARISON OF THE INTENSITY TIME TRACES BY THE SPECTRUM DIVISION METHOD AND THOSE BY FD SIMULATIONS

4.1 Source function

We conduct FD waveform simulations in von Kármán-type random media with $\varepsilon = 0.05$ and $a = 5$ km and $V_0 = 4$ km for a Ricker wavelet source proportional to $(1 - 2\pi^2 f_c^2 t^2) e^{-\pi^2 f_c^2 t^2}$ with a time offset of 0.42 s from the origin time and $f_c = 3$ Hz. When the wave time trace at distance r_1 from the source in a homogeneous medium with the velocity V_0 is given by $u(k_c, r_1, t)$ (see Fig. 4), we calculate the intensity using the Hilbert transform:

$$I(k_c, r_1, t) \equiv \frac{1}{2}\left\{u(k_c, r_1, t)^2 + \mathscr{H}[u(k_c, r_1, t)]^2\right\}. \tag{30}$$

Correcting the geometrical spreading and the travel time, we have the source function at the origin:

$$s(k_c, t) = 4\pi r_1^2 V_0 \times I\left(k_c, r_1, t - \frac{r_1}{V_0}\right). \tag{31}$$

We will use $s(k_c, t)$ in the spectrum division method.

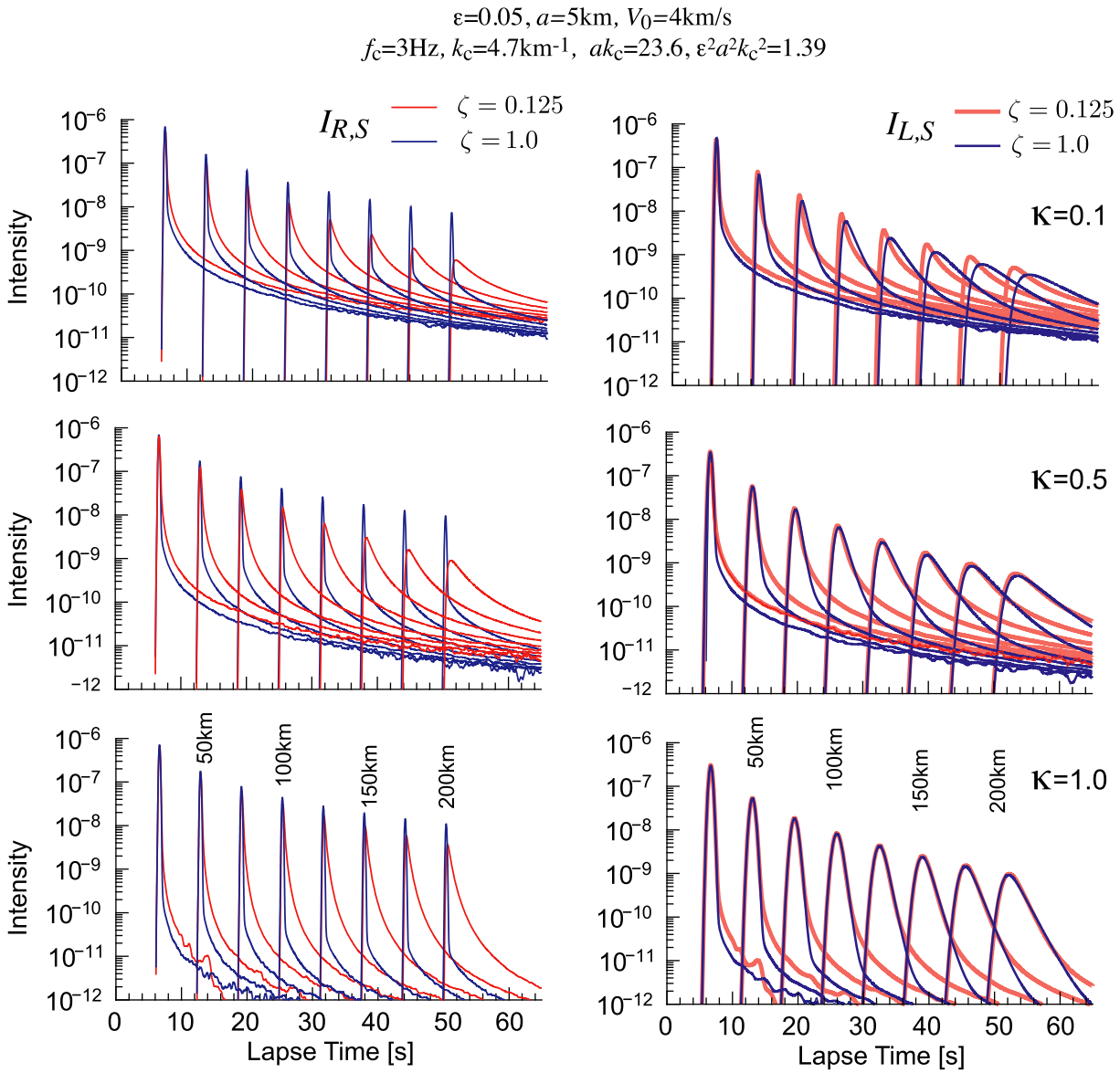

Figure 5. Semi-log plots of $I_{R,S}$ (fine) and $I_{L,S}$ (bold) for $\zeta = 0.125$ (red) and $\zeta = 1.0$ (blue) versus lapse time.

4.2 Synthesis of intensity time traces by the spectrum division method

For a given ζ value, substituting g_S into the RTE (19), we solve it using Monte Carlo (MC) simulations (e.g. Gusev & Abubakirov 1987; Hoshiba 1991; Yoshimoto 2000; Przybilla & Korn 2008; Sens-Schönfelder *et al.* 2009). Particles are randomly shot into various directions, where each particle carries a unit intensity. Particle trajectories are recorded with a time step of $\Delta t = 0.01$ s until 70 s, where the time step is chosen to satisfy $g_{S0} V_0 \Delta t \ll 1$. We count the number of particles at a given lapse time t in a spherical shell of radius r and thickness $\Delta r = 1$ km irrespective of their propagation directions. Dividing the number of particles by the shell volume $4\pi r^2 \Delta r$ and the total number of shots 10^7, we have the response of the scattering medium for a unit source radiation $G_{R,S}$ (20). We evaluate the intensity $I_{R,S}$ (29b) by the convolution of $G_{R,S}$ with the source function $s(k_c, t)$ (31). Then, we evaluate the intensity $I_{L,S}$ (29a) by the convolution of $I_{R,S}$ with the wandering effect w_L and the broadening effect b_L.

On the left panel of Fig. 5, we show semi-log plots of time traces $I_{R,S}$ (fine) for two ζ values. Receiver distances from the source are from 25 to 200 km with a 25 km separation. The time traces resulting from the Monte Carlo simulations are jagged; however, both b_L and w_L work as smoothing filters. $I_{R,S}$ for $\zeta = 1$ (fine blue) has a sharp peak at the onset and a smoothly decaying tail at each travel distance since g_S is small and close to isotropic. Coda of $I_{R,S}$ for $\zeta = 0.125$ (fine red) is larger than that for $\zeta = 1$. $I_{R,S}$ for $\zeta = 0.125$ has a sharp peak at the onset near the source, however, it shows broadening with distance increasing especially for $\kappa = 0.1$ and 0.5. On the right panel of Fig. 5, we show $I_{L,S}$ resulting from the convolution of w_L and b_L with $I_{R,S}$. Difference between $I_{L,S}$ for $\zeta = 1$ (thick blue) and that for $\zeta = 0.125$ (thick red) becomes very small especially around the peak arrival, which is prominent for $\kappa = 0.5$ and 1.0; however, there is some difference between them for $\kappa = 0.1$. There are some difference in coda for $\zeta = 1$ and that for $\zeta = 0.125$ especially for $\kappa = 1.0$. If we focus on the time

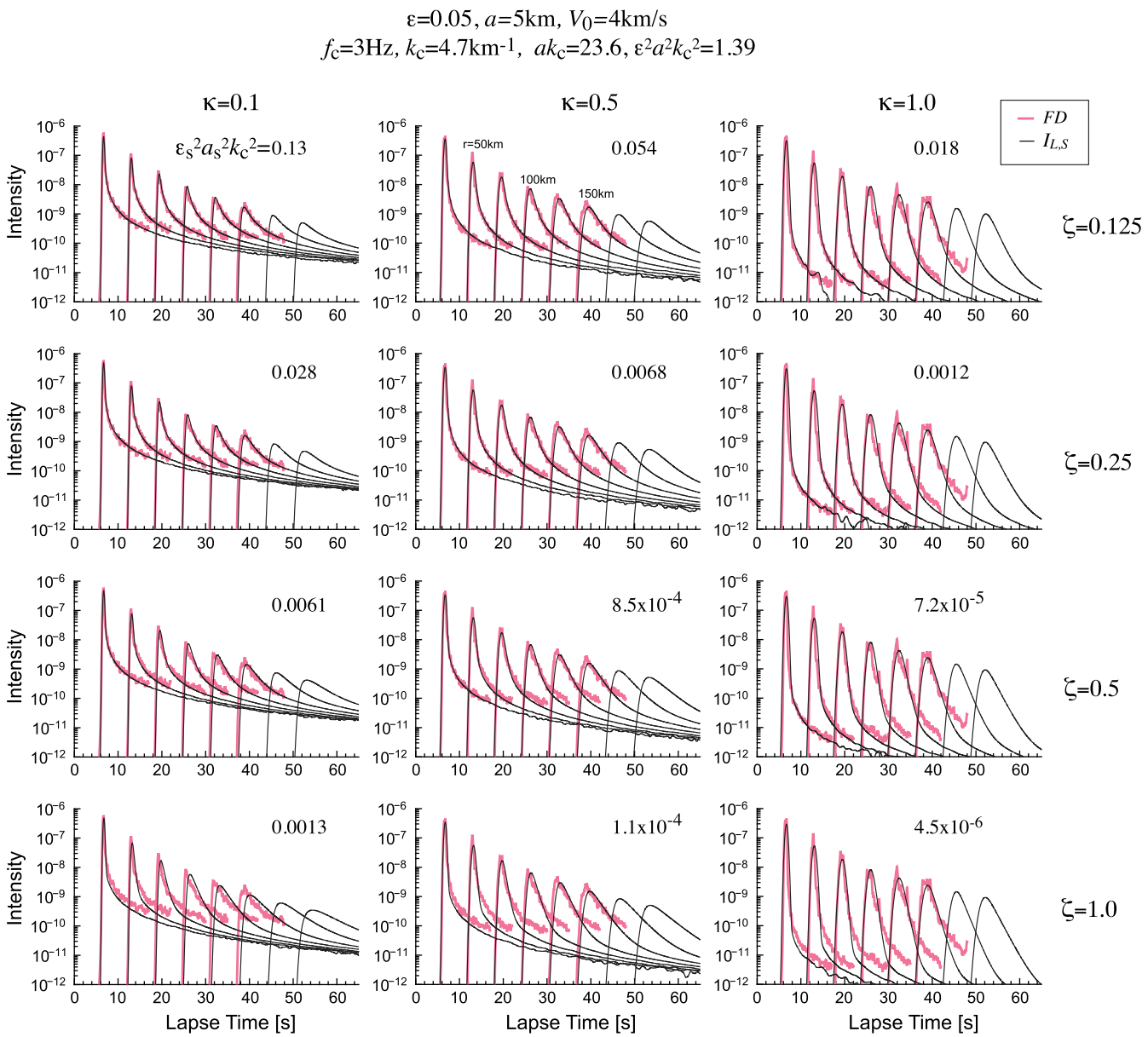

Figure 6. Semi-log plot of intensity versus lapse time for a 3 Hz Ricker wavelet source. Comparison of synthesized intensity trace I_{LS} (black) with averaged FD simulation intensity trace (pink).

trace around the peak, we may say $I_{L,S}$ is rather insensitive to the choice of ζ except $\kappa = 0.1$. For $I_{L,S}$ of $\zeta = 0.125$, the scattering contribution of the short-scale component is large and that of the long-scale component is small; however, it is opposite for the case of $\zeta = 1.0$.

In Fig. 6, we show semi-log plot of $I_{L,S}$ for given κ and ζ values by fine black lines, where $\zeta = 2^{-n}$ for $n = 0 \sim 3$. As shown in the inset, $\varepsilon_S^2 a_S^2 k_c^2$ value increases as ζ decreases. All ζ values satisfy the condition (17); however, it is not satisfied if we put $\zeta = 2^{-4}$. Envelope broadening with travel distance increasing is seen in every case. For a given ζ, coda excitation increases as κ decreases, which reflects the difference in PSDF's. When the spectral roll-off is small as for $\kappa = 0.1$ and 0.5, coda intensity traces at different distances converge to a common decay curve as lapse time increases, which means the uniform distribution of the coda intensity in space. Late coda of $I_{L,S}$ traces are jagged, and the coda intensity for the case of $\kappa = 1.0$ and ζ=0.125 drops at close receivers because the total number of shots in the Monte Carlo simulation is still not large enough.

4.3 Synthesis of intensity time traces by FD simulations

4.3.1 Realization of random media and FD simulations

We conduct FD simulations of the propagation of a 3 Hz Ricker wavelet through random media having the same PSDF. Each random medium is a rectangular parallelepiped with dimensions of 202 km long to the z direction and 133 km wide in the x and y directions (see Fig. 7). The

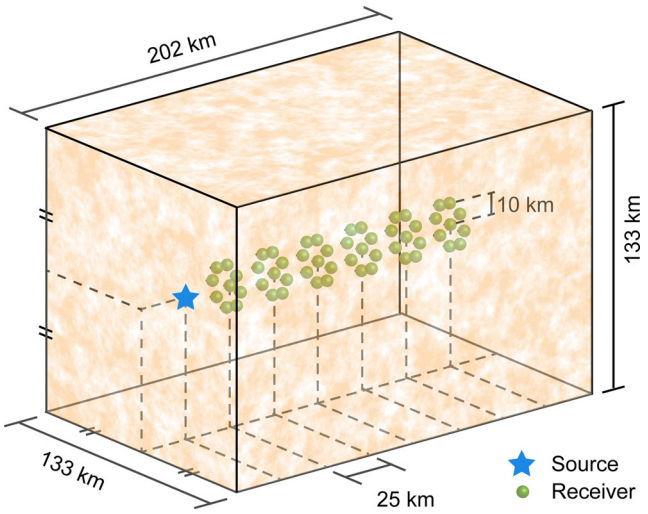

Figure 7. Random medium model space of a rectangular parallelepiped for the FD simulation. Source and receivers are shown by a blue star and green spheres, respectively.

grid spacing is 0.04 km, that is, there are 33 grids per wavelength. Total numbers of grids are 3328, 3328 and 5040 for x, y and z-directions, respectively. Precisions of the FD scheme are 4th and 2nd order in space and time, respectively. We adopt the absorbing condition for all boundaries (Cerjan *et al.* 1985). We show the locations of the source and receivers in Fig. 7. Receiver distances from the source are from 25 to 150 km with a 25 km separation. We set nine receivers at each propagation distance, where one receiver is located on the z-axis and eight receivers are located around it. The distance between the central and a surrounding receiver is 10 km, which is larger than a. The computation is conducted on the Earth Simulator managed by JAMSTEC and is parallelized by using the MPI library along the z-direction (Furumura & Chen 2004). The time interval is 3 ms and the total number of the time step is 16 666, that is, 50 s. Although all the boundaries are absorbing ones, there are waves having a small amplitude reflected from the boundaries. We analyse coda waves of very small amplitudes, so that such small reflected waves might affect the coda amplitude. Therefore, we do not use FD simulation waves after the expected arrival time of each reflected wave at each receiver.

For the realization of a random medium, we use the Fourier transform of the square root of the PSDF with random phases; however, it is difficult to synthesize a random medium of such a large size at once. We first synthesize 96 small random media of 1024^3 grids, and then join them to construct a random medium of a large size. Practically, we conduct the FD simulation for 6 different random media realized by using different random seeds for each κ value. That is, there are 6 realizations $\times$ 9 receivers $=$ 54 wave traces at each propagation distances. We calculate the averaged FD intensity trace by averaging over the 54 intensity traces. The dimension of a realized random medium and the number of random medium realizations are restricted by the CPU power and the capacity of the computer. Precise description and the statistical characteristics of FD simulation wavelets are given in Emoto & Sato (in preparation).

In Fig. 6, we plot averaged intensity time traces by FD simulations by pink line at each travel distance. Envelope broadening with travel distance increasing is seen for every κ value. Long lasting coda waves appear especially for small κ values.

4.3.2 Convergence to the averaged FD intensity trace

We investigate how many FD intensity traces are necessary to obtain a stable averaged FD intensity trace. For a given travel distance, we randomly sort the order of 54 intensity traces and average them one by one. We estimate the number of intensity traces of which the averaged intensity reaches within ± 10 per cent of the final averaged intensity. We conduct the same procedure for 100 different random sort orders, then we average the required numbers at every 0.5 s. Fig. 8 shows the temporal change of the average number of intensity traces. A large number of traces is necessary for $\kappa = 1.0$ compared with the case of $\kappa = 0.1$. Around the peak arrival time, about 40 intensity traces are required. Conversely, about 15 intensity traces are sufficient for the coda. It suggests the self-averaging property of coda that the intensity in one typical realization through a large medium provides the ensemble average intensity.

4.4 Comparison of intensity time traces

4.4.1 Comparison of $I_{L,S}$ and averaged FD intensity time trace

In Fig. 6, we compare the intensity time trace $I_{L,S}$ by the spectrum division method (black) and the averaged FD intensity time trace (pink) for a 3 Hz Ricker wavelet at each travel distance for given κ and different ζ values. We may say the case of $\zeta = 0.125$ shows the best fit from the onset through the peak until coda at each travel distance for every κ value. As ζ increases from 0.25 to 1.0, difference in peak delays increases for $\kappa = 0.1$ and 0.5, and the difference in coda intensities increases for all κ values.

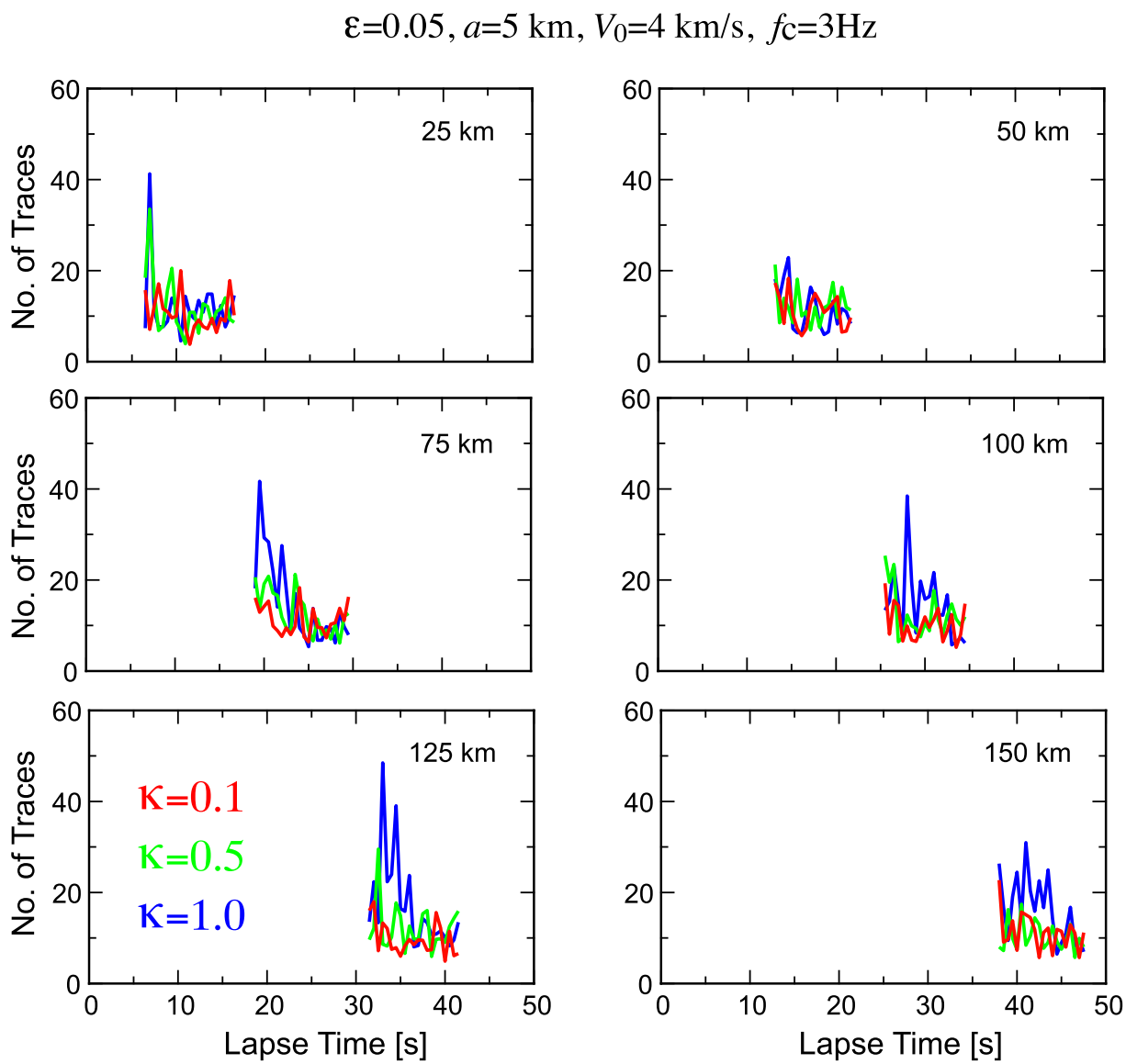

Figure 8. Temporal change of the number of FD intensity traces of which the averaged FD intensity reaches within ±10 per cent of the final averaged FD intensity.

Here we *a priori* suppose $\varepsilon_S^2 a_S^2 k_c^2 = 0.1$ as a typical condition satisfying (17), where ζ varies from 0.082 to 0.14. In Fig. 9, solid lines show $I_{L,S}$ for this condition. These plots also show good coincidence between $I_{L,S}$ and averaged FD intensity traces from the onset through the peak until coda. However, we have not compared the convergence of coda intensity traces to a common decay curve since the lapse time range of the FD simulation is not long enough.

From those comparisons, we may say that the smallest value of ζ satisfying the condition (17) is the best choice, which makes the scattering contribution of the short-scale component large and that of the long-scale component small.

4.4.2 Comparison of I_{La} and averaged FD intensity time trace

Paper I proposed a synthesis for the intensity trace around the peak arrival by the Markov approximation for the long-scale component with the scattering attenuation due to the short-scale component as the lowest correction [Paper I, eq. 41b]:

$$I_{La}(\kappa, k_c, \zeta, r, t) = G_L(\kappa, \zeta, k_c, r, t) e^{-g_{S0}(\kappa, k_c, \zeta) V_0 t} \otimes s(k_c, t)$$
$$= w_L(\kappa, k_c, \zeta, r, t) \otimes b_L(\kappa, k_c, \zeta, r, t) \otimes G_0(r, t) e^{-g_{S0}(\kappa, k_c, \zeta) V_0 t} \otimes s(k_c, t). \quad (32)$$

We show a comparison of I_{La} for $\zeta = 0.5$ (green) and 1.0 (blue) with the averaged FD intensity trace (pink) at each distance in Fig. 10. We see good coincidence between I_{La} and averaged FD intensity traces especially near around the peak at each travel distance; however, there is a large difference between their coda intensities since the positive contribution of wide-angle scattering is not considered. Comparisons for the 2-D case are shown in Sato & Fehler (2016).

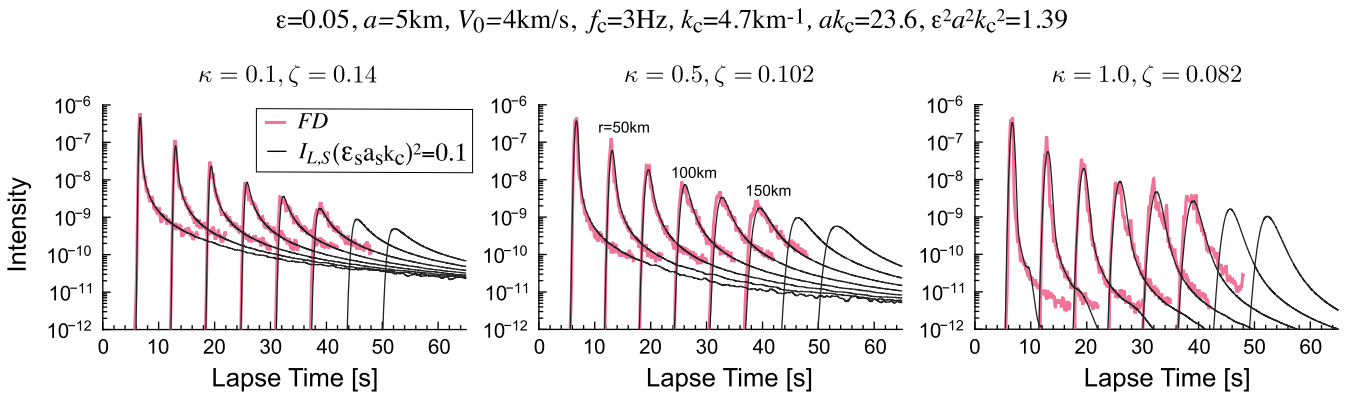

Figure 9. Comparison of the synthesized intensity trace I_{LS} (black) for $\varepsilon_S^2 a_S^2 k_c^2 = 0.1$ with the averaged FD intensity trace (pink) for a 3 Hz Ricker wavelet source at each travel distance.

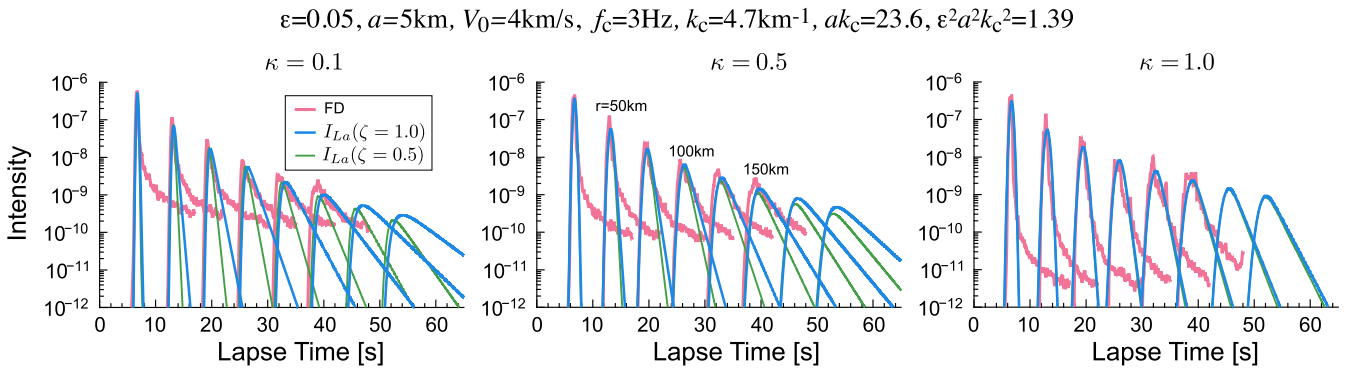

Figure 10. Comparison of the I_{La} trace with the averaged FD intensity trace (pink) for a 3 Hz Ricker wavelet source at each travel distance.

4.4.3 Power-law decay of the maximum intensity versus travel distance

The maximum value of w_L is $\propto r^{-0.5}$ since $t_{WL} \propto r^{0.5}$ and that of b_L is $\propto r^{-2}$ since $t_{ML} \propto r^2$. The maximum value of $I_{R,S}$ decreases according to the geometrical spreading r^{-2} when g_{S0} is small. Therefore, we may expect the maximum value of $I_{L,S} \propto r^{-2}$ at close distances and $\propto r^{-4}$ at large distances. As shown in Fig. 11, the maximum value of the averaged FD intensity (red) shows a power-law decay a little faster than the geometrical decay r^{-2} (dotted line) at travel distance $r < 100$ km, and then it shows more rapid decay approaching to the geometrical and broadening decay r^{-4} (dashed line) as r increases. Those characteristics are well explained by the maximum intensity decay of $I_{L,S}$ (blue dots). There is a slight difference between them for $\kappa = 1.0$. Probably it may reflect the fact that the number of random medium realizations for FD simulations is not large enough for this case.

5 DISCUSSIONS

We have newly proposed the spectrum division method that is useful for the situation where $\varepsilon^2 a^2 k_c^2 \gtrsim O(1)$. We have confirmed the validity of this method by comparison with FD simulations for the situation where $\varepsilon^2 a^2 k_c^2 \sim O(1)$. It will be necessary to compare synthesized intensity

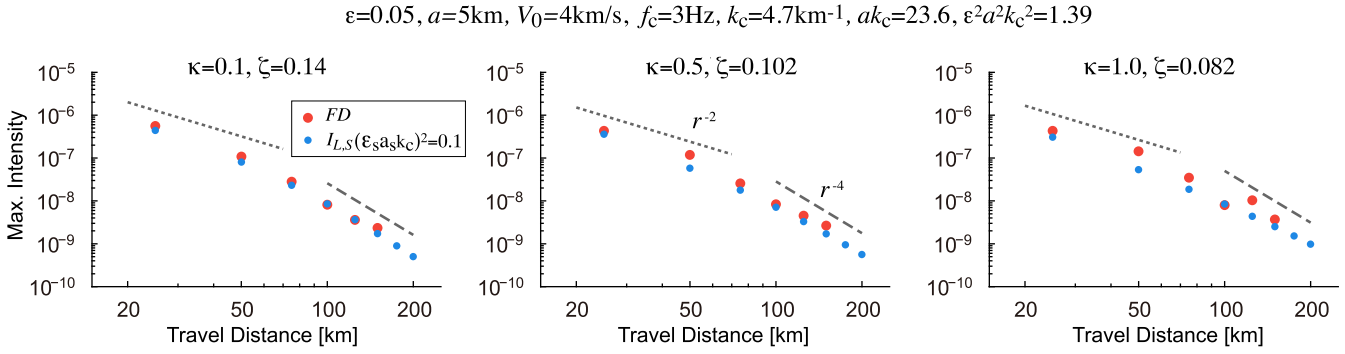

Figure 11. Log–log plot of the maximum intensity versus travel distance. As references, we plot power-law decay r^{-2} (dotted) and r^{-4} (broken).

traces with FD simulations for various parameter sets and different centre frequencies, especially for situations where $\varepsilon^2 a^2 k_c^2 \gg 1$; however, it needs a larger computer power.

When $ak_c > 1$ and $\varepsilon^2 a^2 k_c^2 \sim O(1)$, our syntheses predict that the decrease of the peak intensity varies from the $-$2nd power to the $-$4th power of travel distance as travel distance increases. The resultant power-law decay of the maximum intensity may give a mathematical support for the power-law decay of the maximum amplitude versus distance that has been often used in the magnitude determination of local earthquakes (e.g. Tsuboi 1954). Sato & Fukushima (2013) showed the power-law decay of the maximum intensity versus distance through a fractally random distribution of isotropic scatterers; however, we have shown that the power-law decay is also derived from the broadening effect and the geometrical spreading even in uniform random media. It will be interesting to introduce background velocity increasing with depth, which may lead to a little smaller decay with epicentral distance increasing along the ground surface compared with the present synthesis because of the correction of geometrical spreading.

The number of realizations of small random media and the size of each small random medium for FD simulations are restricted by the CPU power and the memory size in this study. Averaged FD intensity traces for $\kappa = 0.1$ and 0.5 is smooth enough; however, those for $\kappa = 1.0$ look more jagged than others, which means that it is better to use a larger number of random medium realizations to get smoother average FD intensity traces. It is also better to put one receiver at each travel distance (e.g. Fehler *et al.* 2000; Sato & Fehler 2016).

We have used MC simulations to solve the RTE; however, Margerin *et al.* (2016) solved the RTE by using discrete Hankel and Fourier transforms (e.g. Guizar-Sicairos & Gutiérrez-Vega 2004; Baddour 2010; Liemert & Kienle 2012; Baddour & Chouinard 2015). As shown by (5), the RTE can be written as an integral equation. By using the spherical harmonics expansion of non-isotropic scattering coefficient, we can rewrite the RTE as simultaneous equations. Recently Jing *et al.* (2014) presented an advanced numerical technique to solve the simultaneous equations including higher order terms. Their methods will be alternatives to Monte Carlo simulations to solve the RTE.

Sato *et al.* (2004) proposed a method using the intensity trace according to the Markov approximation as a propagator and the transport scattering coefficient as the effective isotropic scattering coefficient in the RTE. As a possible extension, there will be a method using G_L as a propagator and the non-isotropic scattering coefficient g_S in the RTE. The other one is to make a stochastic formulation of the distorted wave Born approximation for scattering by random media for the situation where $\varepsilon^2 a^2 k_c^2 \gtrsim O(1)$. If those are possible, we will be able to calculate the intensity time trace simply using that in the RTE.

6 CONCLUSIONS

For the structure study of the randomly heterogeneous earth medium, it is important to know the propagation characteristics of a seismic wavelet in high-frequencies. As a mathematical model, we have studied the propagation of a scalar wavelet for the spherical radiation from a point source in 3-D von Kármán-type random media with small velocity fractional fluctuation, $\varepsilon^2 \ll 1$. As the centre wavenumber k_c of a wavelet increases in the power-law spectral range $k_c \gg a^{-1}$, we face the situation where $\varepsilon^2 a^2 k_c^2 \gtrsim O(1)$, where the Born approximation fails because of large phase shift. In such a case, we have newly proposed the spectrum division method for the intensity synthesis. Taking ζk_c as a reference, where ζ is a tuning parameter, we divide the random medium spectrum into the short- and long-scale components. Using the RTE with the Born scattering coefficient for the short-scale component, we calculate intensity traces. In parallel, we calculate the broadening and wandering effects applying the Markov approximation to the long-scale component. Finally, we calculate the intensity time trace at a given distance by the convolution of the intensity calculated by the RTE with the broadening and wandering effects, and a source function in the time domain. Resultant intensity time traces show both envelope broadening with travel distance increasing and excitation of long lasting coda waves. When the spectral roll-off is small, coda intensity traces at different distances converge to a common decay curve as lapse time increases, which means the uniform distribution of coda intensity in space. Synthesized intensity traces well explain those of FD simulations from the onset through the peak to coda for the situation where $\varepsilon^2 a^2 k_c^2 \sim O(1)$. Those syntheses will be a theoretical basis for the study of random velocity inhomogeneities in the earth medium from envelopes of high-frequency seismic waves of small earthquakes.

ACKNOWLEDGEMENTS

Authors are grateful to Michael Korn and Ludovic Margerin for their careful review comments and suggestions. FD simulations were conducted on the Earth Simulator at the Japan Agency for marine-Earth Science and Technology (JAMSTEC) under the support of a joint research project between Earthquake Research Institute, the University of Tokyo and Center of Earth Information Science and Technology, 'Numerical simulations of seismic- and tsunami-wave propagation in 3D heterogeneous earth'.

REFERENCES

Aki, K. & Chouet, B., 1975. Origin of coda waves: source, attenuation and scattering effects, *J. geophys. Res.,* **80,** 3322–3342.

Andrews, L.C. & Phillips, R.L., 2005. *Laser Beam Propagation through Random Media,* vol. 52, SPIE Press.

Baddour, N., 2010. Operational and convolution properties of three-dimensional Fourier transforms in spherical polar coordinates, *J. Opt. Soc. Am. A,* **27**(10), 2144–2155.

Baddour, N. & Chouinard, U., 2015. Theory and operational rules for the discrete Hankel transform, *J. Opt. Soc. Am. A,* **32**(4), 611–622.

Calvet, M. & Margerin, L., 2013. Lapse-time dependence of coda Q: anisotropic multiple-scattering models and application to the Pyrenees, *Bull. seism. Soc. Am.,* **103**(3), 1993–2010.

Cerjan, C., Kosloff, D., Kosloff, R. & Reshef, M., 1985. A nonreflecting boundary condition for discrete acoustic and elastic wave equations, *Geophysics,* **50**(4), 705–708.

Chernov, L.A., 1960. *Wave Propagation in a Random Medium* (Engl. trans. by R. A. Silverman)*,* McGraw-Hill.

Emoto, K., Sato, H. & Nishimura, T., 2010. Synthesis of vector-wave envelopes on the free surface of a random medium for the vertical incidence of a plane wavelet based on the Markov approximation, *J. geophys. Res.,* **115,** B08306, doi:10.1029/2009JB006955.

Emoto, K., Sato, H. & Nishimura, T., 2012. Synthesis and applicable condition of vector wave envelopes in layered random elastic media with anisotropic autocorrelation function based on the Markov approximation, *Geophys. J. Int.,* **188,** 325–333.

Fehler, M., Sato, H. & Huang, L.-J., 2000. Envelope broadening of outgoing waves in 2D random media: a comparison between the Markov approximation and numerical simulations, *Bull. seism. Soc. Am.,* **90,** 914–928.

Furumura, T. & Chen, L., 2004. Large scale parallel simulation and visualization of 3D seismic wavefield using the earth simulator, *Comput. Model. Eng. Sci.,* **6,** 153–168.

Guizar-Sicairos, M. & Gutiérrez-Vega, J.C., 2004. Computation of quasi-discrete Hankel transforms of integer order for propagating optical wave fields, *J. Opt. Soc. Am. A,* **21**(1), 53–58.

Gusev, A. & Abubakirov, I., 1996. Simulated envelopes of non-isotropically scattered body waves as compared to observed ones: another manifestation of fractal heterogeneity, *Geophys. J.,* **1001**(127), 9–60.

Gusev, A. & Abubakirov, I., 1999. Vertical profile of effective turbidity reconstructed from broadening of incoherent body-wave pulses-II. Application to Kamchatka data, *Geophys. J. Int.,* **136**(2), 309–323.

Gusev, A.A. & Abubakirov, I.R., 1987. Monte-Carlo simulation of record envelope of a near earthquake, *Phys. Earth planet. Inter.,* **49,** 30–36.

Haney, M.M., Van Wijk, K. & Snieder, R., 2005. Radiative transfer in layered media and its connection to the O'doherty-Anstey formula, *Geophysics,* **70**(1), T1–T11.

Holliger, K., 1996. Upper-crustal seismic velocity heterogeneity as derived from a variety of*P*-wave sonic logs, *Geophys. J. Int.*, **125**(3), 813–829.

Hoshiba, M., 1991. Simulation of multiple-scattered coda wave excitation based on the energy conservation law, *Phys. Earth planet. Inter.,* **67,** 123–136.

Hoshiba, M., 1995. Estimation of nonisotropic scattering in western Japan using coda wave envelopes: application of a multiple nonisotropic scattering model, *J. geophys. Res.,* **100,** 645–657.

Hoshiba, M., Sato, H. & Fehler, M., 1991. Numerical basis of the separation of scattering and intrinsic absorption from full seismogram envelope - A Monte-Carlo simulation of multiple isotropic scattering, *Pap. Meteorol. Geophys.,* **42,** 65–91.

Howe, M.S., 1973. Conservation of energy in random media, with application to the theory of sound absorption by an inhomogeneous flexible plate, *Proc. R. Soc. A,* **331,** 479–496.

Howe, M.S., 1974. A kinetic equation for wave propagation in random media, *Q. J. Mech. Appl. Math.,* **27,** 237–253.

Ishimaru, A., 1997. *Wave Propagation and Scattering in Random Media,* IEEE Press.

Jing, Y., Zeng, Y. & Lin, G., 2014. High-frequency seismogram envelope inversion using a multiple nonisotropic scattering model: Application to aftershocks of the 2008 wells earthquake, *Bull. seism. Soc. Am.,* **104**(2), 823–839.

Kopnichev, Y.F., 1975. A model of generation of the tail of the seismogram, *Dokl. Akad. Nauk SSSR* (Engl. trans.), **222,** 333–335.

Korn, M. & Sato, H., 2005. Synthesis of plane vector wave envelopes in two-dimensional random elastic media based on the Markov approximation and comparison with finite-difference simulations, *Geophys. J. Int.,* **161**(3), 839–848.

Landau, L. & Lifshitz, E., 2003. *Quantum Mechanics,* 3rd edn (Engl. trans. by Sykes, J. B. & Bell, J. S.), Butterworth-Heinemann.

Lee, L.C. & Jokipii, J.R., 1975a. Strong scintillations in astrophysics. I. The Markov approximation, its validity and application to angular broadening, *Astrophys. J.,* **196,** 695–707.

Lee, L.C. & Jokipii, J.R., 1975b. Strong scintillations in astrophysics. II. A theory of temporal broadening of pulses, *Astrophys. J.,* **201,** 532–543.

Liemert, A. & Kienle, A., 2012. Infinite space green's function of the time-dependent radiative transfer equation, *Biomed. Opt. Express,* **3**(3), 543–551.

Mancinelli, N., Shearer, P. & Liu, Q., 2016. Constraints on the heterogeneity spectrum of Earth's upper mantle, *J. geophys. Res.,* **121,** 3703–3721.

Margerin, L., 2005. Introduction to radiative transfer of seismic waves, in *Seismic Earth: Array Analysis of Broadband Seismograms,* vol. 157, pp. 229–252, eds Levander, A. & Nolet, G., Geophysical Monograph-Ameerican Geophysical Union.

Margerin, L., Planès, T., Mayor, J. & Calvet, M., 2016. Sensitivity kernels for coda-wave interferometry and scattering tomography: theory and numerical evaluation in two-dimensional anisotropically scattering media, *Geophys. J. Int.,* **204**(1), 650–666.

McLaughlin, K.L. & Anderson, L.M., 1987. Stochastic dispersion of short-period P-waves due to scattering and multipathing, *Geophys. J. R. astr. Soc.,* **89,** 933–963.

Obara, K. & Sato, H., 1995. Regional differences of random inhomogeneities around the volcanic front in the Kanto-Tokai area, Japan, revealed from the broadening of *S* wave seismogram envelopes, *J. geophys. Res.,* **100,** 2103–2121.

Petukhin, A. & Gusev, A., 2003. The duration-distance relationship and average envelope shapes of small Kamchatka earthquakes, *Pure appl. Geophys.,* **160**(9), 1717–1743.

Przybilla, J. & Korn, M., 2008. Monte Carlo simulation of radiative energy transfer in continuous elastic random media-three-component envelopes and numerical validation, *Geophys. J. Int.,* **173**(2), 566–576.

Rautian, T.G. & Khalturin, V.I., 1978. The use of the coda for determination of the earthquake source spectrum, *Bull. seism. Soc. Am.,* **68,** 923–948.

Rytov, S.M., Kravstov, Y.A. & Tatarskii, V.I., 1989. *Principles of Statistical Radiophysics (Vol. 4) Wave Propagation Through Random Media,* Springer-Verlag.

Saito, T., Sato, H. & Ohtake, M., 2002. Envelope broadening of spherically outgoing waves in three-dimensional random media having power-law spectra, *J. geophys. Res.,* **107**(B5), ESE 3-1–ESE 3-15.

Saito, T., Sato, H., Ohtake, M. & Obara, K., 2005. Unified explanation of envelope broadening and maximum-amplitude decay of high-frequency seismograms based on the envelope simulation using the Markov approximation: Forearc side of the volcanic front in northeastern Honshu, Japan, *J. geophys. Res.,* **110,** B01304, doi:10.1029/2004JB003225.

Sato, H., 1977. Energy propagation including scattering effects: Single isotropic scattering approximation, *J. Phys. Earth,* **25,** 27–41.

Sato, H., 1984. Attenuation and envelope formation of three-component seismograms of small local earthquakes in randomly inhomogeneous lithosphere, *J. geophys. Res.,* **89,** 1221–1241.

Sato, H., 1989. Broadening of seismogram envelopes in the randomly inhomogeneous lithosphere based on the parabolic approximation: Southeastern Honshu, Japan, *J. geophys. Res.,* **94,** 17 735–17 747.

Sato, H., 1995. Formulation of the multiple non-isotropic scattering process in 3-D space on the basis of energy transport theory, *Geophys. J. Int.,* **121,** 523–531.

Sato, H., 2008. Synthesis of vector-wave envelopes in 3-D random media characterized by a nonisotropic Gaussian ACF based on the Markov approximation, *J. geophys. Res.,* **113,** B08304, doi:10.1029/2007JB005524.

Sato, H., 2016. Envelope broadening and scattering attenuation of a scalar wavelet in random media having power-law spectra, *Geophys. J. Int.,* **204**(1), 386–398.

Sato, H. & Fehler, M.C., 2016. Synthesis of wavelet envelope in 2-D random media having power-law spectra: comparison with FD simulations, *Geophys. J. Int.,* **207**(1), 333–342.

Sato, H. & Fukushima, R., 2013. Radiative transfer theory for the fractal structure and power-law decay characteristics of short-period seismograms, *Geophys. J. Int.,* **195,** 1831–1842.

Sato, H., Fehler, M. & Saito, T., 2004. Hybrid synthesis of scalar wave envelopes in two-dimensional random media having rich short-wavelength spectra, *J. geophys. Res.,* **109,** B06303, doi:10.1029/2003JB002673.

Sato, H., Fehler, M. & Maeda, T., 2012. *Seismic Wave Propagation and Scattering in the Heterogeneous Earth,* 2nd edn, Springer Verlag.

Sawazaki, K., Sato, H. & Nishimura, T., 2011. Envelope synthesis of short-period seismograms in 3-D random media for a point shear dislocation source based on the forward scattering approximation: application to small strike-slip earthquakes in southwestern Japan, *J. geophys. Res.,* **116,** B08305, doi:10.1029/2010JB008182.

Sens-Schönfelder, C., Margerin, L. & Campillo, M., 2009. Laterally heterogeneous scattering explains Lg blockage in the Pyrenees, *J. geophys. Res.,* **114,** B07309, doi:10.1029/2008JB006107.

Shearer, P.M. & Earle, P.S., 2004. The global short-period wavefield modelled with a Monte Carlo seismic phonon method, *Geophys. J. Int.,* **158,** 1103–1117.

Shiomi, K., Sato, H. & Ohtake, M., 1997. Broad-band power-law spectra of well-log data in Japan, *Geophys. J. Int.,* **130,** 57–64.

Shishov, V.I., 1974. Effect of refraction on scintillation characteristics and average pulse shape of pulsars, *Sov. Astron.,* **17,** 598–602.

Sreenivasiah, I., Ishimaru, A. & Hong, S.T., 1976. Two-frequency mutual coherence function and pulse propagation in a random medium: an analytic solution to the plane wave case, *Radio Sci.,* **11,** 775–778.

Takahashi, T., Sato, H. & Nishimura, T., 2007. Strong inhomogeneity beneath Quaternary volcanoes revealed from the peak delay analysis of *S*-wave seismograms of microearthquakes in northeastern, Japan, *Geophys. J. Int.,* **168,** 90–99.

Takahashi, T., Sato, H., Nishimura, T. & Obara, K., 2009. Tomographic inversion of the peak delay times to reveal random velocity fluctuations in the lithosphere: method and application to northeastern Japan, *Geophys. J. Int.,* **178**(47), 1437–1455.

Tripathi, J., Sato, H. & Yamamoto, M., 2010. Envelope broadening characteristics of crustal earthquakes in northeastern Honshu, Japan, *Geophys. J. Int.,* **182**(2), 988–1000.

Tsuboi, C., 1954. Determination of the Gutenberg-Richter's magnitude of earthquakes occurring in and near Japan, *Zisin (in Japanese),* **7,** 185–193.

Wegler, U., Korn, M. & Przybilla, J., 2006. Modeling full seismogram envelopes using radiative transfer theory with born scattering coefficients, *Pure appl. Geophys.,* **163**(2–3), 503–531.

Williamson, I.P., 1972. Pulse broadening due to multiple scattering in the interstellar medium, *Mon. Not. R. Astron. Soc.,* **157,** 55–71.

Wu, R.S., Xu, Z. & Li, X.P., 1994. Heterogeneity spectrum and scale-anisotropy in the upper crust revealed by the German Continental Deep-Drilling (KTB) holes, *Geophys. Res. Lett.,* **21,** 911–914.

Yoshimoto, K., 2000. Monte-Carlo simulation of seismogram envelope in scattering media, *J. geophys. Res.,* **105,** 6153–6161.

Yoshimoto, K., Sato, H. & Ohtake, M., 1997. Three-component seismogram envelope synthesis in randomly inhomogeneous semi-infinite media based on the single scattering approximation, *Phys. Earth planet. Inter.,* **104,** 37–61.

Zeng, Y., Su, F. & Aki, K., 1991. Scattering wave energy propagation in a random isotropic scattering medium 1. Theory, *J. geophys. Res.,* **96,** 607–619.